PERGAMON

International Journal of Heat and Mass Transfer 45 (2002) 3369–3382

International Journal of HEAT and MASS TRANSFER

www.elsevier.com/locate/ijhmt

Hot-electron blast induced by ultrashort-pulsed lasers in layered media

D.Y. Tzou [a,*], J.K. Chen [b], J.E. Beraun [b]

[a] *Department of Mechanical and Aerospace Engineering, University of Missouri-Columbia, Columbia, MO 65211, USA*

[b] *Laser Effects Research Branch, Directed Energy Directorate, Air Force Research Laboratory, Kirtland AFB, NM 87117, USA*

Received 10 August 2001; received in revised form 10 January 2002

Abstract

Femtosecond laser heating on metals produces a blasting force in the sub-picosecond domain, which exerts on the metal lattices along with the non-equilibrium heat flow from hot electrons. Such a hot-electron blast depends on both temperature and temperature gradient in the electron gas, resulting in pronounced effects in multi-layered metal films due to discontinuous heat transfer and load transmission across the interface. This work employs the parabolic two-step model to study the effect of the hot-electron blast in multi-layered thin metal films. Dominating physical parameters are identified to characterize the ultrafast heating and deformation across the interface.

1. Introduction

Ultrafast lasers with pulse durations of the order of sub-picosecond (ps, 10^{-12} s) to femtosecond (fs, 10^{-15} s) domain possess exclusive capabilities in limiting the undesirable spread of the thermal process zone in the heated sample. In addition to the demonstrated applications for structural monitoring of thin metal films [1,2], laser micromachining [3] and patterning [4], structural tailoring of microfilms [5], and laser synthesis and processing in thin-film deposition [6], recent applications of femtosecond lasers have well spanned in all disciplines of physics, chemistry, biology, medicine, and optical technology [7–10]. The non-contact nature of femtosecond lasers, in addition, has made them an ideal candidate for precise thermal processing of functional nanophase materials [11,12].

While femtosecond lasers have been attracting worldwide interest in science and engineering, it has been a constant trend that the heating intensity is continuously increased to improve the processing power. To date, femtosecond lasers can deliver energy levels spanning the electromagnetic spectrum from the X-rays to T-rays (10^{12} Hz radiation), generating optical peak powers as colossal as petawatts (10^{15} W) [13,14]. Success of high-energy femtosecond lasers in real applications relies on three factors. First, such ultrashort-pulsed lasers must be well characterized, including development of the experimental techniques and determination of the pulse width, the laser-beam heating profile, and the detailed history of laser-material interactions in the sub-picosecond domain [15–17]. Second, reliable microscale heat transfer models must be in place to describe the various microstructural interaction effects that are activated during the ultrafast transient in the pico/femtosecond domain [18–29]. Third, combining the fundamental understandings thus developed, including both laser characterizations and model developments, the most important task in real applications is prevention of thermal damage. Note that ultrafast damage induced by the sub-picosecond pulses is intrinsically different from that induced by the long-pulse or continuous lasers. For the latter, laser damage is caused by the elevated temperatures resulting from the continuous pumping of photon energy into the processed sample. The ''damage threshold'' termed in heating by long-pulse lasers, therefore, is often referred to as the laser intensity that drives the heated spot to the melting temperature. Thermal

* Corresponding author. Tel.: +1-573-882-4060; fax: +1-573-884-5090.

E-mail address: tzour@missouri.edu (D.Y. Tzou).

0017-9310/02/$ - see front matter
PII: S0017-9310(02)00053-4

Nomenclature

C	volumetric heat capacity (J m^{-3} K^{-1})
d	fraction between 0 and 1
d_{ij}	deformation potential
E	modulus of elasticity (Pa)
G	phonon–electron coupling factor (W m^{-3} K^{-1})
H	non-dimensional value of G
i	nodal number
J	laser fluence (J m^{-2})
K	non-dimensional thermal diffusivity of electrons at room temperature
k	thermal conductivity (W m^{-1} K^{-1})
L	non-dimensional film thickness
M	nodal number
l	film thickness (m)
$\mathbf{p}$	vector of energy state variables (eV)
R	surface reflectivity, dimensionless
R_X	ratio of property X, $X^{(\mathrm{II})}/X^{(\mathrm{I})}$
S	energy absorption rate (W m^{-3})
S_F	Fermi surface (m^2)
T	temperature (K)
T_0	initial temperature (K)
t	time (s)
U	non-dimensional displacement of acoustic phonons
u	displacement of acoustic phonons (m)
t	physical time (s)
v	mean electron velocity (m s^{-1})
x	one-dimensional space variable (m)
$x_{i,j,l,m}$	$i,j,l,m = 1,2,3$. Spatial coordinates in the x_1, x_2, and x_3 directions (m)

Greek symbols

β	non-dimensional time
δ	optical depth (m)
ε	Cauchy strain (nm nm^{-1})
ε_F	Fermi energy (J)
Λ	electron blast coefficient (J m^{-3} K^{-2})
θ	non-dimensional temperature
ρ	mass density of acoustic phonons (kg m^{-3})
σ	Cauchy stress (Pa)
ξ	non-dimensional space

Subscripts and superscripts

e	electron
l	lattice
p	pulse
max	maximum value
n	nodal number of the time grid
0	room temperature (300 K) or reference state
(j)	$j \equiv \mathrm{I}, \mathrm{II}$. Medium number
(i)	nodal number

damage induced by ultrashort pulses in the picosecond domain, on the other hand, occurs after the heating pulse is over [30]. Field induced multi-photon ionization produces free electrons that are rapidly accelerated by the laser pulse. Absorbing energy from the impinging photons in the femtosecond domain, these free electrons mobilize and ionize neighboring atoms through high-frequency collisions, which generates more electrons. The hot electrons transmit thermal energy to phonons through phonon–electron coupling, resulting in a new thermal property, called the electron–phonon coupling factor, for microscale heat transfer in metals [15–26]. This process continues until a critical density of hot electrons is reached. Under a sufficiently high intensity of heating, in fact, experimental results [13,14] have shown that the ultrafast damage involves shattering of a thin material layer (from the heated surface) without a clear signature of thermal damage by excessive temperature. Rather than the melting damage developed at high temperature, obviously, there exists a new driving force that brings about such ultrafast damage; probably in only a few picoseconds after heating is applied.

The recent work on the hot-electron blast [31] sheds light on revealing the fundamental mechanisms of ultrafast deformation in the "cold" lattices (acoustic phonons) during non-equilibrium heating on metals. The deformation potential, resulting from the energy integrals of electrons on the Fermi surface, was found proportional to the electron temperature squared, giving rise to a blasting force that depends on both the temperature and temperature gradient in the electron gas. For a 0.1 μm gold film heated by a 100 fs laser, such a blasting force lasts for about 1.5 ps [32]. Compression was initially developed in the acoustic phonons due to rapid bombardment of hot electrons. The subsequent tension across the thermomechanical wavefront, however, may be so strong that the metal lattice can be destroyed before reaching the damage threshold by melting. Electrons and phonons are highly non-equilibrium during the hot-electron blast, with electron being excited to several thousand degrees while phonons remain almost thermally undisturbed. Damage thus developed in the cold lattices closely resembles the experimental observations [13,14] of surface shattering induced by intense ultrashort lasers.

Now that the hot-electron blast is found significant under intensified heating, ultrafast deformation needs to be addressed altogether in non-equilibrium heating of electrons and phonons. This is particularly true for submicron films because the magnitude of deformation may easily reach a fraction of the film thickness on the microscopic level. This work extends the hot-electron blast model [31,32] to study the ultrafast deformation in layered metal films. Since the hot electron blast strongly depends on the temperature gradient in the electron gas, particular emphasis is placed on the interfacial area where the temperature gradient experiences an abrupt change in transition from one metal film to another.

2. Ultrafast deformation and heating

For metals heated by ultrashort-pulsed lasers, deformation of acoustic phonons during the first few picoseconds is driven by the hot electron blast. In terms of the general dynamical equations of thermoelasticity [31], the equations of motion can be expressed as

$$\rho\frac{\partial^2 u_i}{\partial t^2}-E_{ijlm}\frac{\partial^2 u_l}{\partial x_j\partial x_m}=\Lambda_{ij}\left(2T_e\frac{\partial T_e}{\partial x_j}\right),$$
$$\text{where } \Lambda_{ij}=\frac{1}{32\pi}\frac{\partial}{\partial\varepsilon_F}\int\frac{d_{ij}(\mathbf{p})\,dS_F}{v}. \tag{1}$$

In Eq. (1), a repeated index in a single term (such as j, l, and m) refers to summations (from 1 to 3 for all j, l, and m). The first term reflects the inertia effect of the acoustic phonons. The second term results from the stress gradient,

$$\frac{\partial\sigma_{ij}}{\partial x_j}=\frac{\partial}{\partial x_j}(E_{ijlm}\varepsilon_{lm})=E_{ijlm}\frac{\partial^2 u_l}{\partial x_j\partial x_m},$$

which assumes a constant modulus of lattice elasticity and a small deformation of acoustic phonons during the picosecond transient. The driving force induced by hot electrons, the term on the right-hand side of Eq. (1), is a unique feature derived from the dynamical theory of thermoelasticity. Up to the second order of $(T_e/T_F)^2$, with T_F representing the Fermi temperature (6.42×10^4 K for gold), the blasting force is proportional to the gradient of the electron-temperature squared, recalling that $\partial(T_e^2)/\partial x_j=2T_e\partial T_e/\partial x_j$. Such a product form explicitly shows the strong dependence of the blasting force on both temperature and temperature gradient in the electron gas [32].

The proportional constant, Λ_{ij} in Eq. (1), unfortunately, is difficult to evaluate because the number of free electrons in various metals has not been sufficiently clear yet. For noble metals such as gold, the number of free electrons is usually taken as one per atom and the number of free electrons is taken as a fraction of the valence electrons in the s-band [20]. With an electron density states on the order of 10^{-2}–10^{-1} levels per electron volt (eV) per atom, which is typical for most metals, the value of Λ_{ij} should be of the order of 10–10^2 J m^{-3} K^{-2}. Comparing to the result estimated on the order of magnitude as well [31], $\Lambda_{ij}\sim C_{e0}/T_0$ with C_{e0} being the heat capacity of electrons at room temperature T_0. For gold, $\Lambda_{ij}\sim C_{e0}/T_0\cong 70$ J m^{-3} K^{-2}, which lies within the aforementioned threshold.

In spite of the familiar form, Eq. (1) originated from the dynamical Hamiltonian principle [33,34] has several unique features. First, the modulus of elasticity (E_{ijlm}) may undergo a significant change as a result of the electron loop in the phonon self-energy function. Such a change is proportional to the integral of d_{ij} and d_{lm} over the Fermi surface, yielding a quantity proportional to $(T_e/T_F)^2$. Under the same assumption that $(T_e/T_F)\ll 1$, obviously, the modulus of elasticity can be assumed invariant ($E_{ijlm}\sim$ constant). Second, effect of stress relaxation due to thermal expansion of the metal lattices appears later than that of the hot-electron blast [32]. A direct use of Hookes' law without considering the thermal expansion effects, therefore, is made in the dynamical equations of motion when describing the ultrafast deformation of acoustic phonons.

2.1. Electron–phonon interactions

Ultrafast heating involves high-rate heat flow from electrons to phonons in the picosecond domain. Electrons have much smaller heat capacity than phonons, by two to three orders of magnitude, depending on the temperature of electrons. When heated by photons (lasers), electrons first shoot to several hundreds to thousands degrees within a few picoseconds without disturbing the metal lattices. This stage is termed non-equilibrium heating [20–22,26] due to the large difference of temperatures in electrons and phonons. The lattice (phonon) temperature then increases as a result of phonon–electron coupling, resulting in a new thermal property termed phonon–electron coupling factor G. In forms parallel to Eq. (1), the energy equations describing the continuous energy flow from hot electrons to phonons during non-equilibrium heating can be written as:

$$C_e(T_e)\frac{\partial T_e}{\partial t}=\frac{\partial}{\partial x_j}\left[k_e(T_e,T_l)\frac{\partial T_e}{\partial x_j}\right]-G(T_e-T_l)+S(x_j,t);$$
$$C_l\frac{\partial T_l}{\partial t}=G(T_e-T_l),\quad \text{where } C_e(T_e)=C_{e0}\left(\frac{T_e}{T_0}\right)$$
$$\text{and } k_e(T_e,T_l)=k_0\left(\frac{T_e}{T_l}\right). \tag{2}$$

Heat transport in the electron gas is assumed diffusive (following Fourier's law) and effect of conduction

through the metal lattices is neglected due to the optical depth (of laser penetration) in metals typically on the order of 0.01 μm. Eq. (2), consequently, is termed the parabolic two-step model [20–22].

The intensity of heat flow from electrons to phonons is assumed proportional to the temperature difference between electrons and phonons, $T_e - T_l$. The proportional constant, G, is insensitive to temperature. The value of G ranges from 10^{14} to 10^{16} W m^{-3} K^{-1} for most metals [20]. For gold, for example, $G \cong 2.6 \times 10^{16}$ W m^{-3} K^{-1}. Thermal properties of phonons are much less sensitive to temperature than those of electrons. metal lattice display Heating by ultrashort-pulsed lasers involves more than a heat flux specified at the surface.

The energy absorption rate, $S(x_j, t)$ in Eq. (2), describes the Gaussian distribution employing the normalized autocorrelation function of the laser pulse and a full width at half maximum (FWHM) based pulse duration (t_p). The initial heating time, consequently, is shifted from 0 to $-2t_p$, with the resulting Gaussian profile peaking at time 0 [17,26]. In the case of one-dimensional heating, assuming constant optical properties of metals, the energy absorption rate can be approximated by

$$S(x,t) = 0.94J\left(\frac{1-R}{\delta t_p}\right)\exp\left[-\frac{x}{\delta} - 4\ln(2)\left(\frac{t}{t_p}\right)^2\right] \tag{3}$$

with x denoting the major axis of thermomechanical response. For multi-dimensional heating, the bracketed quantities also involve the directional energy absorption rates in different directions [35].

3. Thin-film heating and deformation

Direct dependence of the hot-electron blast on the temperature gradient in the electron gas warrants a careful study of ultrafast heating and deformation in the interfacial area between dissimilar films. Revealed by the heat transfer analysis assuming rigid conductors [22], temperature gradient in the electron gas may develop a strong discontinuity near the interface at extremely short times. The abrupt change of temperature gradient implies a strong blasting force in transition from one medium to another, which may result in unexpected delamination failure in cold lattices, at a temperature much lower than the melting temperature.

A sub-micron metal film consisting of two material layers are considered to illustrate the general effects of the hot-electron blast across the interface. The total thickness of the two-layer film remains to be of the order of 0.1 μm, which is much smaller than the diameter of the heated spot on the metal surface, justifying the use of

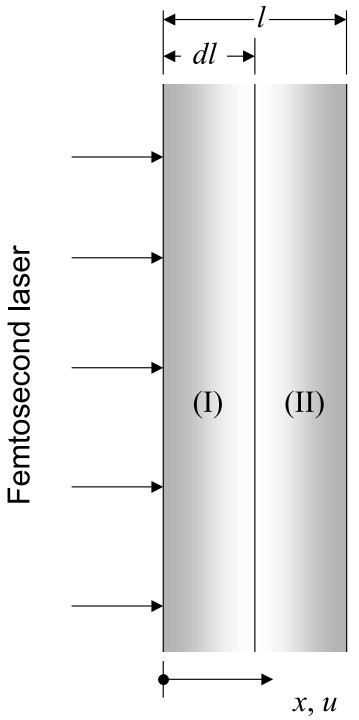

Fig. 1. Femtosecond-laser heating on a double-layered metal film of thickness L with an interface located at $x = dl$ ($0 < d < 1$).

one-dimensional models in describing ultrafast heating and deformation. The coordinate system is sketched in Fig. 1, which illustrates a double-layered metal film with an interface at $x = dl$ ($0 < d < 1$). The dynamical equations of motion in each material layers are reduced from Eq. (1):

$$\begin{aligned}
\rho^{(I)}\frac{\partial^2 u^{(I)}}{\partial t^2} - E^{(I)}\frac{\partial^2 u^{(I)}}{\partial x^2} &= 2\Lambda^{(I)}\left(T_e^{(I)}\frac{\partial T_e^{(I)}}{\partial x}\right),\\
\rho^{(II)}\frac{\partial^2 u^{(II)}}{\partial t^2} - E^{(II)}\frac{\partial^2 u^{(II)}}{\partial x^2} &= 2\Lambda^{(II)}\left(T_e^{(II)}\frac{\partial T_e^{(II)}}{\partial x}\right).
\end{aligned} \tag{4}$$

Likewise, the two-step energy equations are reduced from Eq. (2):

$$\begin{aligned}
C_{e0}^{(I)}\left(\frac{T_e^{(I)}}{T_0}\right)\frac{\partial T_e^{(I)}}{\partial t} &= k_{e0}^{(I)}\frac{\partial}{\partial x}\left[\left(\frac{T_e^{(I)}}{T_l^{(I)}}\right)\frac{\partial T_e^{(I)}}{\partial x}\right]\\
&\quad - G^{(I)}\left(T_e^{(I)} - T_l^{(I)}\right) + 0.94J\left(\frac{1-R}{\delta t_p}\right)\\
&\quad \times \exp\left[-\frac{x}{\delta} - 4\ln(2)\left(\frac{t}{t_p}\right)^2\right],\\
C_l^{(I)}\frac{\partial T_l^{(I)}}{\partial t} &= G^{(I)}\left(T_e^{(I)} - T_l^{(I)}\right);
\end{aligned} \tag{5}$$

$$C_{e0}^{(II)}\left(\frac{T_e^{(II)}}{T_0}\right)\frac{\partial T_e^{(II)}}{\partial t}=k_{e0}^{(II)}\frac{\partial}{\partial x}\left[\left(\frac{T_e^{(II)}}{T_l^{(II)}}\right)\frac{\partial T_e^{(II)}}{\partial x}\right]-G^{(II)}\left(T_e^{(II)}-T_l^{(II)}\right)+0.94J\left(\frac{1-R}{\delta t_p}\right)\times\exp\left[-\frac{x}{\delta}-4\ln(2)\left(\frac{t}{t_p}\right)^2\right],$$

$$C_l^{(II)}\frac{\partial T_l^{(II)}}{\partial t}=G^{(II)}\left(T_e^{(II)}-T_l^{(II)}\right). \tag{6}$$

In Eq. (4), $E^{(I,II)}\equiv E_{1111}^{(I,II)}$ and $\Lambda^{(I,II)}\equiv\Lambda_{11}^{(I,II)}$ are the only components of E_{ijlm} and Λ_{ij} that appear in the one-dimensional equations of motion.

In ultrafast deformation neglecting the stress relaxation effect in thermal expansion of the metal lattices, the strain-free and stress-free conditions at the film surfaces are mutually implied:

$$\frac{\partial u^{(I)}}{\partial x}=0 \text{ at } x=0 \quad \text{and} \quad \frac{\partial u^{(II)}}{\partial x}=0 \text{ at } x=l. \tag{7}$$

Energy losses from the front and back surfaces of the film, in addition, is negligible during the picosecond transient, implying

$$\frac{\partial T_e^{(I)}}{\partial x}=\frac{\partial T_l^{(I)}}{\partial x}=0 \text{ at } x=0 \quad \text{and}$$
$$\frac{\partial T_e^{(II)}}{\partial x}=\frac{\partial T_l^{(II)}}{\partial x}=0 \text{ at } x=l. \tag{8}$$

Displacement and stress of acoustic phonons, mechanically, are assumed continuous across the interface,

$$u^{(I)}=u^{(II)} \quad \text{and} \quad E^{(I)}\frac{\partial u^{(I)}}{\partial x}=E^{(II)}\frac{\partial u^{(II)}}{\partial x} \text{ at } x=dl. \tag{9}$$

Thermodynamically, on the other hand, temperature and heat flux of electrons are assumed continuous at $x=dl$,

$$T_e^{(I)}=T_e^{(II)} \quad \text{and}$$
$$k_{e0}^{(I)}\left(\frac{T_e^{(I)}}{T_l^{(I)}}\right)\frac{\partial T_e^{(I)}}{\partial x}=k_{e0}^{(II)}\left(\frac{T_e^{(II)}}{T_l^{(II)}}\right)\frac{\partial T_e^{(II)}}{\partial x} \text{ at } x=dl. \tag{10}$$

Both electrons and phonons are assumed disturbed from an equilibrium temperature

$$T_e^{(I)}=T_l^{(I)}=T_e^{(II)}=T_l^{(II)}=T_0 \quad \text{as } t=-2t_p, \tag{11}$$

with the initial time $(-2t_p)$ resulting from the description of FWHM duration of the laser pulse. Mechanically, at last, both media are assumed disturbed from a stationary state

$$u^{(I)}=u^{(II)}=0 \quad \text{and} \quad \frac{\partial u^{(I)}}{\partial t}=\frac{\partial u^{(II)}}{\partial t}=0 \text{ as } t=-2t_p. \tag{12}$$

In passing, note that the relaxation behavior (finite speed of heat propagation) for heat transport through acoustic phonons may be present during the short-time transient, which will add additional wave terms in the phonon (second) equations in Eqs. (5) and (6). Since the typical relaxation time of phonon-to-phonon collisions is of the order of 10 ps for most metals, and our primary concerns are the hot-electron blast during the first few picoseconds, such wave effects are excluded in the present model. Even with the conduction effect implemented in the energy equations for the metal lattices, in fact, we have shown that the phonon wave effect becomes noticeable only after several tens of picoseconds.

3.1. Dominating parameters

Eqs. (4)–(12) involve a large number of parameters from both thermal and mechanical fields. To extract the dominating parameters, non-dimensional parameters based on medium (I) are further introduced to characterize the ultrafast heating and deformation

$$\xi=\frac{x}{\delta}, \quad \beta=\frac{t}{t_p}, \quad \theta_{e(l)}^{(I,II)}=\frac{T_{e(l)}^{(I,II)}}{T_0},$$
$$U^{(I,II)}=\frac{u^{(I,II)}}{\left(\Lambda^{(I)}T_0^2t_p^2/\rho^{(I)}\delta\right)}, \quad Y=\frac{E^{(I)}/\rho^{(I)}}{(\delta/t_p)^2},$$
$$S_0=0.94J\left(\frac{1-R}{\delta C_{e0}^{(I)}T_0}\right), \quad H=\frac{G^{(I)}t_p}{C_{e0}^{(I)}},$$
$$K=\frac{k_{e0}^{(I)}t_p}{C_{e0}^{(I)}\delta^2}, \quad C=\frac{C_{e0}^{(I)}}{C_l^{(I)}}, \quad L=\frac{l}{\delta}. \tag{13}$$

In terms of these parameters, Eqs. (4)–(12) become

$$\frac{\partial^2U^{(I)}}{\partial\beta^2}-Y\frac{\partial^2U^{(I)}}{\partial\xi^2}=2\theta_e^{(I)}\frac{\partial\theta_e^{(I)}}{\partial\xi}, \tag{14}$$

$$\frac{\partial^2U^{(II)}}{\partial\beta^2}-Y\left(\frac{R_E}{R_\rho}\right)\frac{\partial^2U^{(II)}}{\partial\xi^2}=2\left(\frac{R_\Lambda}{R_\rho}\right)\theta_e^{(II)}\frac{\partial\theta_e^{(II)}}{\partial\xi}, \tag{15}$$

$$\theta_e^{(I)}\frac{\partial\theta_e^{(I)}}{\partial\beta}=K\frac{\partial}{\partial\xi}\left(\frac{\theta_e^{(I)}}{\theta_l^{(I)}}\frac{\partial\theta_e^{(I)}}{\partial\xi}\right)-H\left(\theta_e^{(I)}-\theta_l^{(I)}\right)+S_0\exp\left[-\xi-4\ln(2)\beta^2\right],$$
$$\frac{\partial\theta_l^{(I)}}{\partial\beta}=HC\left(\theta_e^{(I)}-\theta_l^{(I)}\right), \tag{16}$$

$$\theta_e^{(II)}\frac{\partial\theta_e^{(II)}}{\partial\beta}=K\left(\frac{R_k}{R_{C_e}}\right)\frac{\partial}{\partial\xi}\left(\frac{\theta_e^{(II)}}{\theta_l^{(II)}}\frac{\partial\theta_e^{(II)}}{\partial\xi}\right)-H\left(\frac{R_G}{R_{C_e}}\right)\times\left(\theta_e^{(I)}-\theta_l^{(I)}\right)+\frac{S_0}{R_{C_e}}\exp\left[-\xi-4\ln(2)\beta^2\right],$$
$$\frac{\partial\theta_l^{(II)}}{\partial\beta}=H\left(\frac{R_GR_{C_{el}}}{R_{C_l}}\right)\left(\theta_e^{(II)}-\theta_l^{(II)}\right), \tag{17}$$

$$\frac{\partial\theta_{\mathrm{e}}^{(\mathrm{I})}}{\partial\xi}=\frac{\partial\theta_{\mathrm{l}}^{(\mathrm{I})}}{\partial\xi}=\frac{\partial U^{(\mathrm{I})}}{\partial\xi}=0 \text{ at } \xi=0,$$
$$\frac{\partial\theta_{\mathrm{e}}^{(\mathrm{II})}}{\partial\xi}=\frac{\partial\theta_{\mathrm{l}}^{(\mathrm{II})}}{\partial\xi}=\frac{\partial U^{(\mathrm{II})}}{\partial\xi}=0 \text{ at } \xi=L, \tag{18}$$

$$\theta_{\mathrm{e}}^{(\mathrm{I})}=\theta_{\mathrm{e}}^{(\mathrm{II})},\quad \frac{\theta_{\mathrm{e}}^{(\mathrm{I})}}{\theta_{\mathrm{l}}^{(\mathrm{I})}}\frac{\partial\theta_{\mathrm{e}}^{(\mathrm{I})}}{\partial\xi}=R_k\frac{\theta_{\mathrm{e}}^{(\mathrm{II})}}{\theta_{\mathrm{l}}^{(\mathrm{II})}}\frac{\partial\theta_{\mathrm{e}}^{(\mathrm{II})}}{\partial\xi},$$
$$U^{(\mathrm{I})}=U^{(\mathrm{II})},\quad \frac{\partial U^{(\mathrm{I})}}{\partial\xi}=R_E\frac{\partial U^{(\mathrm{II})}}{\partial\xi} \text{ at } \xi=dL, \tag{19}$$

$$\theta_{\mathrm{e}}^{(\mathrm{I})}=\theta_{\mathrm{l}}^{(\mathrm{I})}=\theta_{\mathrm{e}}^{(\mathrm{II})}=\theta_{\mathrm{l}}^{(\mathrm{II})}=1,\quad U^{(\mathrm{I})}=U^{(\mathrm{II})}=0,$$
$$\text{and}\quad \frac{\partial U^{(\mathrm{I})}}{\partial\beta}=\frac{\partial U^{(\mathrm{II})}}{\partial\beta}=0 \text{ as } \beta=-2. \tag{20}$$

Expectedly, various ratios (R's) exist due to the presence of two metals films in contact:

$$R_\rho=\frac{\rho^{(\mathrm{II})}}{\rho^{(\mathrm{I})}},\quad R_E=\frac{E^{(\mathrm{II})}}{E^{(\mathrm{I})}},\quad R_\Lambda=\frac{\Lambda^{(\mathrm{II})}}{\Lambda^{(\mathrm{I})}},$$
$$R_k=\frac{k_{\mathrm{e}0}^{(\mathrm{II})}}{k_{\mathrm{e}0}^{(\mathrm{I})}},\quad R_{C_{\mathrm{e}}}=\frac{C_{\mathrm{e}0}^{(\mathrm{II})}}{C_{\mathrm{e}0}^{(\mathrm{I})}},\quad R_{C\mathrm{l}}=\frac{C_{\mathrm{l}}^{(\mathrm{II})}}{C_{\mathrm{l}}^{(\mathrm{I})}},\quad R_G=\frac{G^{(\mathrm{II})}}{G^{(\mathrm{I})}}. \tag{21}$$

In addition to the ratios of thermomechanical properties, clearly, ultrafast heating and deformation are characterized by four parameters. They are (1) parameter K, the squared ratio of the diffusion length of electrons at room temperature to the thermal penetration depth, (2) parameter H, the amount of thermal energy exchange between electrons and phonons per volume in one pulse t_{p} relative to the volumetric heat capacity of electrons at room temperature, (3) parameter C the ratio of volumetric specific heat between electrons and phonons at room temperature, and (4) parameter Y, the squared velocity ratio between the dilatational wave speed $\sqrt{E^{(\mathrm{I})}/\rho^{(\mathrm{I})}}$ and (δ/t_{p}). The non-dimensional intensity (S_0) and film thickness (L), in addition, are two external parameters characterizing the heating condition and geometry of the metal film.

Analytical solutions to Eqs. (14)–(20) are quite intractable due to the temperature-dependent thermomechanical properties and the nonlinear blasting force from hot electrons. The finite difference-differential equations are therefore developed to solve these coupled equations numerically.

4. Differential-difference formulation

The differential-difference approach retains the time derivatives in a partial differential equation while discretizing the spatial derivatives according to the finite difference schemes. This procedure results in a set of coupled ordinary differential equations that are established at every node discretizing the physical domain in the computational space.

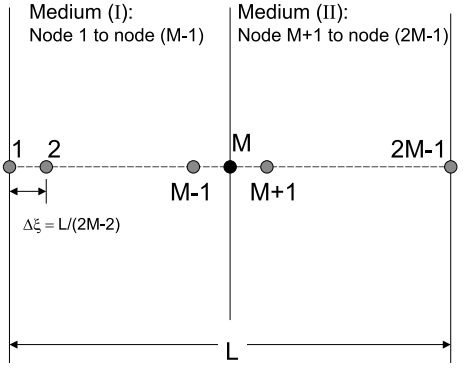

Fig. 2. Nodal sequence used to discretize the double-layered film of thickness L : A total of $(2M-1)$ nodes with the interfacial node assigned at M.

Fig. 2 illustrates the nodal sequence used in the differential-difference analysis for Eqs. (14)–(17). The interfacial node is placed at M, with nodal number from 1 to $(M-1)$ assigned to the quantities in medium (I) and nodal number from $(M+1)$ to $(2M-1)$ assigned to the quantities in medium (II). For a general node i located in medium (I), Eqs. (14) and (16) are used, resulting in

$$\frac{\mathrm{d}^2U_{(i)}}{\mathrm{d}\beta^2}-Y\left[\frac{U_{(i+1)}+U_{(i-1)}-2U_{(i)}}{(\Delta\xi)^2}\right]=\theta_{\mathrm{e}(i)}\left[\frac{\theta_{\mathrm{e}(i+1)}-\theta_{\mathrm{e}(i-1)}}{\Delta\xi}\right],\quad i=2,\ldots,M-1, \tag{22}$$

$$\theta_{\mathrm{e}(i)}\frac{\mathrm{d}\theta_{\mathrm{e}(i)}}{\mathrm{d}\beta}=K\left\{\frac{\theta_{\mathrm{e}(i)}}{\theta_{\mathrm{l}(i)}}\left[\frac{\theta_{\mathrm{e}(i+1)}+\theta_{\mathrm{e}(i-1)}-2\theta_{\mathrm{e}(i)}}{(\Delta\xi)^2}\right]+\frac{1}{\theta_{\mathrm{l}(i)}}\left(\frac{\theta_{\mathrm{e}(i+1)}-\theta_{\mathrm{e}(i-1)}}{2\Delta\xi}\right)^2-\frac{\theta_{\mathrm{e}(i)}}{\theta_{\mathrm{l}(i)}^2}\left[\frac{\left(\theta_{\mathrm{e}(i+1)}-\theta_{\mathrm{e}(i-1)}\right)}{2\Delta\xi}\times\frac{\left(\theta_{\mathrm{l}(i+1)}-\theta_{\mathrm{l}(i-1)}\right)}{2\Delta\xi}\right]\right\}-H\left(\theta_{\mathrm{e}(i)}-\theta_{\mathrm{l}(i)}\right)+S_0\exp\left[-(i-1)\Delta\xi-4\ln(2)\beta^2\right],\quad i=2,\ldots,M-1, \tag{23}$$

$$\frac{\mathrm{d}\theta_{\mathrm{l}(i)}}{\mathrm{d}\beta}=HC\left(\theta_{\mathrm{e}(i)}-\theta_{\mathrm{l}(i)}\right),\quad i=2,\ldots,M-1. \tag{24}$$

The central-difference formulas are employed for both first and second order derivatives with respect to space (ξ) in these equations. With $\Delta\xi=L/(2M-2)$, Eqs. (22)–(24) represent a set of nonlinearly coupled ordinary differential equations for $U_{(i)}$, $\theta_{\mathrm{e}(i)}$, and $\theta_{\mathrm{l}(i)}$ at node i. Similar equations can be obtained for node i located in medium (II), by the use of Eqs. (15) and (17) instead. All spatial derivatives are the same as those in Eqs. (22)–(24), except for the appearance of the property ratios (Rs') in correspondence.

Eq. (20) serves as the initial conditions for the ordinary differential equations thus obtained. The zero-slope conditions in Eq. (18) are ensured by imposing

$$\begin{aligned}&\theta_{e(1)}=\theta_{e(2)},\quad \theta_{l(1)}=\theta_{l(2)},\quad U_{(1)}=U_{(2)}\\&\quad\text{(for boundary conditions at } \xi=0),\\&\theta_{e(2M-1)}=\theta_{e(2M-2)},\quad \theta_{l(2M-1)}=\theta_{l(2M-2)},\\&\quad U_{(2M-1)}=U_{(2M-2)}\quad\text{(for boundary conditions at } \xi=L).\end{aligned}\tag{25}$$

The finite difference forms for the interfacial conditions in Eq. (19), for node M at $\xi=d$, at last, are

$$\begin{aligned}\theta_{e(M)}&=\frac{1}{1+R_k}\left(R_k\theta_{e(M+1)}+\theta_{e(M-1)}\right),\\U_{(M)}&=\frac{1}{1+R_E}\left(R_E U_{(M+1)}+U_{(M-1)}\right).\end{aligned}\tag{26}$$

5. Numerical results

Ultrafast deformation in a double-layered film heated by a 100 fs ($t_p=0.1ps$) laser is studied to illustrate the effect of the hot-electron blast. The laser fluence is taken as $J=500$ J m^{-2}. The optical depth of penetration is taken as $\delta=15.3$ nm, which is a typical value for visible lights. Such an ultrafast laser directly heats a gold film of thickness 0.05 μm (50 nm, medium (I) in Fig. 1) that is padded with a chromium film of equal thickness (medium (II) in Fig. 1). The total thickness of the double-layered film is thus 0.1 μm (100 nm), which is a particular case of $d=1/2$ in Eq. (19). Thermophysical properties for gold and chromium are listed in Table 1 [22], along with all the non-dimensional parameters calculated from Eqs. (13) and (21). Note that the values of R_A and R_{C_e} are identical due to the same initial temperature (T_0) assumed.

The system of coupled ordinary differential equations (ODEs), exemplified by Eqs. (22)–(24) for medium (I), is solved by the use of the IVPAG sub-routine in IMSL [36]. It employs the fifth-order Gear's backward differentiation formula (BDF) to suppress the stiffness in such a set of nonlinearly coupled ODEs, along with the adaptive algorithm that continuously decreases the time interval until the maximum error in the changes of θ_e, θ_l, and U is less than 1.0×10^{-5}. The adaptively adjusted time step ($\Delta\beta$) turns out to be less than 0.05 for all cases.

5.1. Non-equilibrium heating

Fig. 3 shows the temperature distributions of electrons (Fig. 3(a)) and lattices (Fig. 3(b)) in the double-layered film. The interface is located at $x=50$ nm as marked by the dashed vertical line in Fig. 3. Physical scales of temperatures ($\theta_{e,l}$), time (t), and space (x) are recovered for the time being in accordance with $T_{e,l}=\theta_{e,l}\times300$ K, $t=\beta\times0.1$ ps, and $x=\xi\times15.3$ nm. As the number of nodes increases from 9 ($M=5$), 29 ($M=15$), to 99 ($M=50$), the highly desirable patterns of uniform convergence is present at all times in both Fig. 3(a) (for electron temperature) and Fig. 3(b) (for lattice temperature). The results of $M=50$ (99 nodes), which will be used in all numerical computations in this work, agree very well with those obtained by the semi-implicit Crank–Nicholson scheme employing 400 grid points [22]. In presence of mixed high-order diffusion (two-step model for heat transfer) and mechanical waves (for load transmission), clearly, the differential-difference method provides a reliable approach for calculating the electron and phonon temperatures in layered films.

Based on the uniform convergence of the differential-difference method thus demonstrated, we focus our attention on the solid curves in Figs. 3(a) and (b) (the case of $M=50$). Electron temperature peaks at 3727 K at the heated surface ($x=0$) toward the end of the laser pulse ($t=0.1$ ps), as shown in Fig. 3(a). Electron temperature decays slowly in the gold film ($0<x<50$ nm), but drops more rapidly in the chromium film ($50\text{ nm}<x<100$ nm). In transition from the gold layer to the chromium layer, an abrupt increase of the temperature gradient ($\partial T_e/\partial x$) is present at the interface. Such a discontinuity, as shown in Eq. (26), is dictated by the value of R_k. Electron temperature decreases with time in

Table 1
Thermophysical properties for gold and chromium: reflectivity, $R=0.93$; optical depth of penetration, $\delta=15.3$ nm

Properties	Gold	Chromium
Thermal conductivity, k_{e0} (W m^{-1} K^{-1})	315	94
Lattice heat capacity, C_l (J m^{-3} K^{-1})	2.5×10^6	3.3×10^6
Electron heat capacity, C_{e0} (J m^{-3} K^{-1})	2.1×10^4	5.8×10^4
Electron–phonon coupling factor, G (W m^{-3} K^{-1})	2.6×10^{16}	4.2×10^{17}
Density, ρ (kg m^{-3})	19,300	7190
Modulus of elasticity, E (GPa)	77.97	279.45
Electron-blast coefficient, Λ (J m^{-3} K^{-2})	70	193.3

$H=0.124$, $K=6.41$, $S_0=341.3$, $Y=1.71\times10^{-4}$, $C=8.4\times10^{-3}$, $R_\rho=0.37$, $R_E=3.584$, $R_A=2.76$, $R_k=0.298$, $R_{C_e}=2.76$, $R_G=16.15$, $R_{C_l}=1.32$, $L=6.536$.

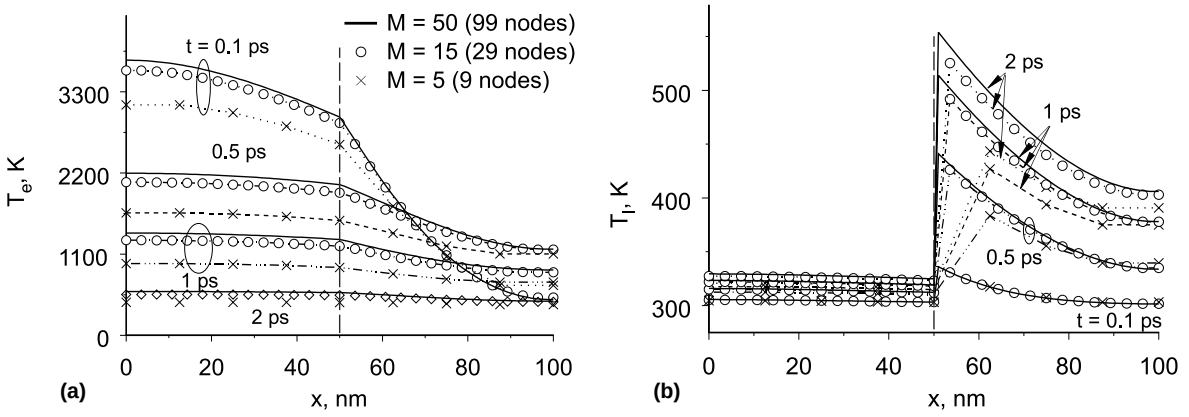

Fig. 3. Uniform convergence of (a) electron temperature and (b) lattice temperature as the number of nodes increases from 29 to 99.

the gold layer due to the effect of heat diffusion in the electron gas and the constant heat flow from hot electrons to metal lattices (phonon–electron interactions). In the chromium layer, however, electron temperatures established at later times (0.5, 1, and 2 ps) may become higher than the early-time temperature (0.1 ps) due to the combined effect of continuous heat diffusion and phonon–electron interactions. The lattice temperature continuous increases with time, in both gold and chromium films, due to constant heating of acoustic phonons by electrons, as shown in Fig. 3(b). The lattice temperature increases in an almost uniform fashion in the gold film, from 303 to about 324 K as the response time increases from 0.1 to 2 ps. Across the interface at $x = 50$ nm, the lattice temperature drastically increases, with the peak value increased from 336 K (at 0.1 ps), 441 K (0.5 ps), 514 K (1 ps), to 554 K (2 ps). Again, a clear discontinuity of the temperature gradient $(\partial T_l/\partial x)$ is developed at the interface, which may evolve into the major cause for lattice delamination if lasting for a long time (beyond tens of picoseconds, not shown). The difference of electron (Fig. 3(a)) and phonon (Fig. 3(b)) temperatures, by as much as one order of magnitude at short times, gives a strong flavor of non-equilibrium heating during the picosecond transient.

Distributions of electron and phonon temperatures in the space and time domains are presented Fig. 4, which compares the results in a double-layered film (0.05 μm gold and 0.05 μm chromium) to those in a single-layered film (0.1 μm gold) under the same heating conditions. The single-layered results, Fig. 4(a) for electron temperature and Fig. 4(c) for lattice temperature, employ 30 nodes that discretize the entire film ($l = 0.1$ μm or $L = 6.536$). Thermomechanical properties for gold are used in Eqs. (22)–(24), with nodal number i running from 2 to 29. The initial and boundary conditions remain the same as Eqs. (18) and (20), with both superscripts (I) and (II) now referring to gold. For a single-layered film, the uniformly convergent results can be achieved by using much less nodes due to the absence of a material interface. The double-layered results, Fig. 4(b) for electron temperature and Fig. 4(d) for lattice temperature, are general representations of Figs. 3(a) and (b) in three dimensions. Comparing Fig. 4(a) to Fig. 4(b), electron temperatures of gold in the double-layered film $(0 < \xi < 3.268)$ decay at much faster rates than that in the single-layered film. The phonon–electron coupling factor (G value) of chromium is about one order of magnitude larger than that of gold, resulting in a much lower temperature in the chromium layer $(3.268 < \xi < 6.536)$. The discontinuities displayed in Figs. 4(b) and (d) are located at the interface $(\xi = 3.268)$ between the chromium and gold layers. The advantage of padding a chromium layer behind the gold layer is clear when comparing the lattice temperatures of gold in Fig. 4(c) (single-layer) and (d) (double-layer, in the domain $0 < \xi < 3.268$). In the presence of a chromium layer, under the same total thickness, the lattice temperature of gold in the double-layered film $(0 < \xi < 3.268)$ is more uniform and significantly lower than that in the single-layered film. Though having a lower thermal conductivity, clearly, the chromium layer possessing a larger value of the phonon–electron coupling factor (G) serves as the "heat sink" to the gold layer.

5.2. Electron blast

A negative temperature gradient in the electron gas $(\partial T_e/\partial x < 0)$, as clearly shown in Figs. 3 and 4, results in a negative blasting force, $2T_e(\partial T_e/\partial x) < 0$. In parallel to Figs. 4 and 5 compares the hot-electron blasts in the single- and double-layered films. Note that the blasting force vanishes at the front $(\xi = 0)$ and back $(\xi = 6.536)$ surfaces of the film due to the insulated boundary conditions imposed in Eq. (18). The 0.1 ps (t_p) laser produces a blasting force that lasts for about 0.2 ps

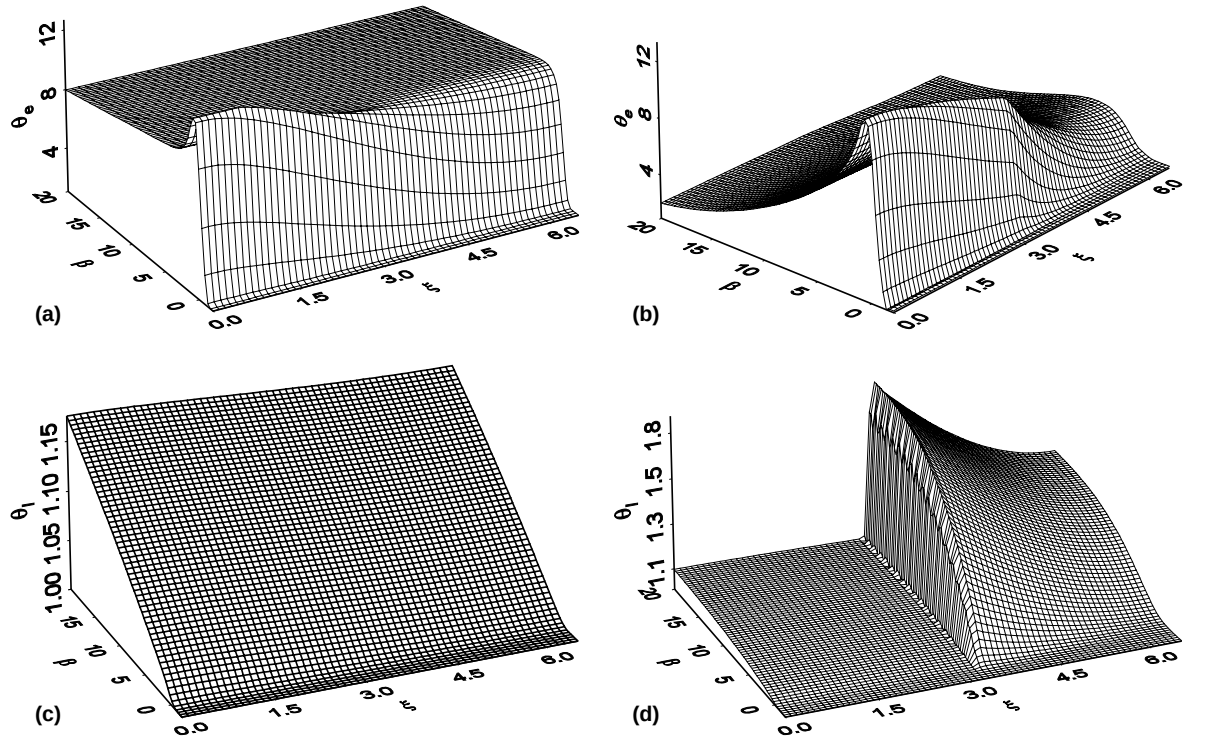

Fig. 4. Distributions of (a) electron temperature in a single-layered film, (b) electron temperature in a double-layered film, (c) lattice temperature in a single-layered film, and (d) lattice temperature in a double-layered film.

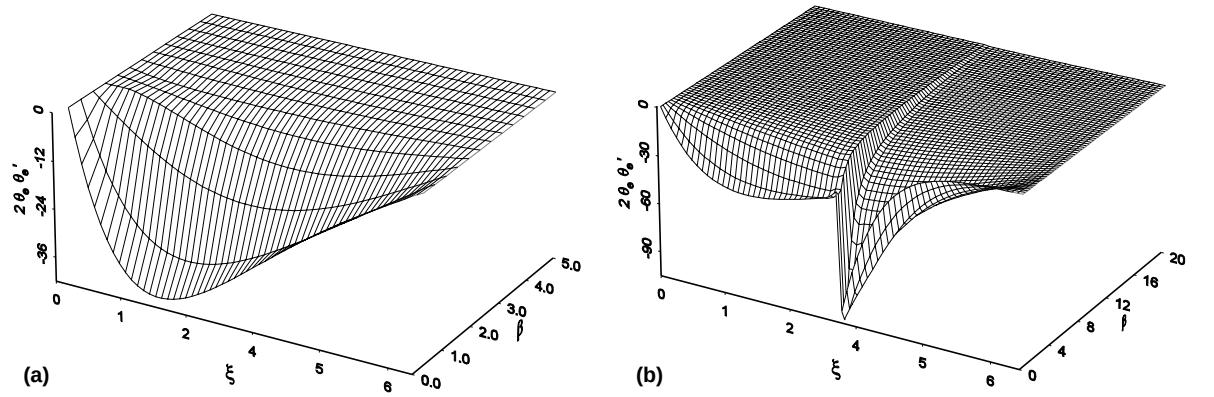

Fig. 5. Hot-electron blast in (a) the single-layered film and (b) the double- layered film with same thickness ($L = 6.536$).

$(0 < \beta < 2)$, Fig. 5(a). The location experiencing maximum blasting force is closer to the front (heated) surface at early times, reaching $[2T_e(\partial T_e/\partial x)]_{max} = -39.4$ at $\xi = 1.69$ as $= 0.28$ ($t = 0.028$ ps). Such a location rapidly shifts toward the center of the film, reducing to $[2T_e \times (\partial T_e/\partial x)]_{max} = -6.03$ at $\xi = 3.27$ as β increases to 1.79. The electron blast in the double-layered film behaves somewhat similar, Fig. 5(b). As the response time (β) increases from 0.24 to 1.59, within the gold layer in $0 < \xi < 3.268$, the location possessing maximum blasting force shifts more rapidly from $\xi = 1.63$ (middle of the gold film) with $[2T_e(\partial T_e/\partial x)]_{max} = -42.28$ to $\xi = 3.23$ (very close to the interface) with $[2T_e(\partial T_e/\partial x)]_{max} = -15.9$. The discontinuity across the interface in the double-layered film, however, results in drastically increased blasting forces in the chromium layer $(3.268 < \xi < 6.536)$. The location possessing maximum blasting force drifts in the vicinity of the interface, reducing from the value of $[2T_e(\partial T_e/x)]_{max} = -98.2$ at $\xi = 3.30$ as $\beta = 0.24$ to $[2T_e(\partial T_e/\partial x)]_{max} = -57.13$ at $\xi = 3.37$ as $\beta = 1.59$.

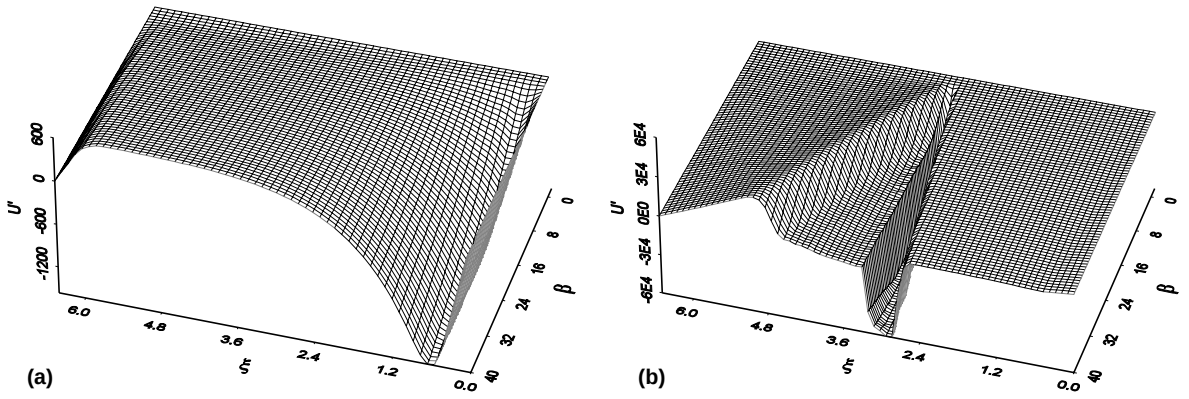

Fig. 6. Ultrafast straining (U') in (a) the single-layered film and (b) the double-layered film with same thickness ($L = 6.536$).

The discontinuous change of the hot-electron blasting force across the interface prolongs to about 2 ps ($\beta = 20$), with the major blast remains to be in tenths of a picosecond.

5.3. Ultrafast straining

Negative blasting forces shown in Fig. 5 produce negative strains (compressions) near the heated surface. This is clearly shown in Fig. 6(a) for a single-layered film in a broader time domain (β) from 0 to 40 ($t = 4$ ps). The maximum compression occurs near the characteristic line of mechanical waves located at $\xi = \sqrt{Y}\beta$, or $\xi \cong 0.013077\beta$ for $Y = 1.71 \times 10^{-4}$ in gold (see Table 1). Effect of high-order diffusion in hot electrons, however, extends the maximum compression a little over the characteristic wavefront ($\xi \cong 0.523$ as $\beta = 40$), reaching $U'_{\max} = -1573.2$ at $\xi = 0.56$ as $\beta = 40$. The magnitude of compressive strains rapid decreases after crossing the characteristic wavefront, eventually switching into tensile strain in approaching the back surface of the film. The tensile region thus developed covers more than half of the film thickness, peaking at 601.37 at $\xi = 5.37$ as $\beta = 40$. Since metals are weaker in general when resisting tension, the tensile region developed in the rear portion of the film would be more detrimental. Should the intensity of femtosecond-laser heating be sufficiently strong, ultrafast damage would occur in the rear portion of the film, rather than the front portion directed heated by the laser.

The discontinuous blasting force across the material interface, as shown earlier in Fig. 5(b), results in more capricious deformation patterns as described in Fig. 6(b). Large compression (U') is rapidly formed in the vicinity of the interface, reaching the order of 10^4–10^5 as $\beta = 40$, which is so strong that the compressible strain existing at the characteristic wavefront in the gold film ($\xi \cong 0.523$ as $\beta = 40$) becomes almost invisible. The characteristic wavefront is switched from gold to chromium after crossing the interface, producing a maximum *tensile* strain $U' \cong 2.78 \times 10^4$ that peaks at $(\xi, \beta) = (5.04, 40)$ in the domain of $0 < \beta < 40$. The characteristic wavefront in the chromium layer is calculated by

$$x = \left(\sqrt{\frac{E}{\rho}}\right)_{\text{chromium}} t \quad \text{or} \quad \xi = \sqrt{\frac{R_E}{R_\rho}}\sqrt{Y}\beta, \tag{27}$$

where parameter Y is based on gold. Along with the values of R_E and R_ρ listed in Table 1, Eq. (27) results in $\xi \cong 0.040699\beta$ in the chromium layer, which gives $\xi \cong 1.63$ as $\beta = 40$. Since the chromium layer is measured from the interface ($\xi = 3.268$), the characteristic wavefront in chromium is located at $\xi \cong 4.89$ as $\beta = 40$, which is the peak of the tensile strain shown in Fig. 6(b).

To convert the value of $\partial U/\partial\xi(U')$ to $\partial u/\partial x$ (Cauchy strain), multiply the value of U' by $1.922 \times 10^{-10}\Lambda$. For gold and chromium, referring to Table 1, this conversion results in $(\partial u/\partial x)_{\text{gold}} \cong 1.345 \times 10^{-8}U'$ and $(\partial u/\partial x)_{\text{chromium}} \cong 3.715 \times 10^{-8}U'$. For the maximum tensile strains shown in Fig. 6, both occur in the rear portion of the film, $(\partial u/\partial x)_{\text{gold,max}} \cong 8.088 \times 10^{-6}$ and $(\partial u/\partial x)_{\text{chromium,max}} \cong 1.034 \times 10^{-3}$ that are in equivalence to $\sigma_{\text{gold,max}} \cong 0.63$ MPa and $\sigma_{\text{chromium,max}} \cong 288.9$ MPa according to the elastic moduli given in Table 1. Although the failure data under high stain rates (approximately 10^8–10^9 s^{-1} in the present problem) are not available yet, these levels of strain and stress at the most exaggerated state would damage the chromium film in the picosecond domain. While serving as the heat sink to the directly heated gold film, therefore, potential damage in the chromium layer is noteworthy. The quantitative estimates so far are made with $J = 500$ J m^{-2}, which is only a tenth of the laser fluence used for materials removal by femtosecond lasers [13,14,32]. The stress and strain levels in the picosecond domain will increase accordingly should the processing power of the femtosecond lasers be increased.

5.4. Effects of H, Y, K and C

In all comparisons made below, Fig. 6(b) shall be used as the base curve with all the parameters listed in Table 1. Since parameters H, Y, K, and C are defined based on medium (I) under direct laser heating, referring to Eq. (13), varying their values is equivalent to replacing the gold layer by another one with the corresponding properties in medium (I).

Enhanced diffusion in the electron gas and metal lattices, which is indeed the major role that the phonon–electron coupling factor (G) plays during the phonon–electron interactions, exaggerates the deformation field in the vicinity of the material interface and the characteristic wavefront. As the value of H increases by two orders of magnitude ($H = 12.4$ comparing to $H = 0.124$ in Fig. 6(b)), implying a hundred times increase of the G value under the same heating condition, the near field deformation becomes wiggling in approaching the material interface ($\xi \to 3.268$) and the wavefront ($\xi \to 0.040699\beta$ measured from the interface). This is clearly shown in Fig. 7(a). While perverting all the general features in Fig. 6(b), the value of U' is reduced by several times as the value of H increases from 12.4 to 0.124. The case of $H = 12.4$ corresponds to the value of G in niobium or vanadium.

A larger value of Y implies a faster dilatational wave speed, again, under the same heating conditions. The thermomechanical disturbance carried by the characteristic waves, consequently, travels more frequently in the double-layered film with the same thickness. In the same domain of $0 < \beta < 40$ ($0 < t < 4$ ps), as shown in Fig. 7(b), there exists a clear branch of the reflected wave emanating from the rear surface ($\xi = 6.536$). The reflected waves are also present in the neighborhood of the interface ($\xi = 6.536$). Interactions between the oncoming and reflected waves broaden the compressive deformation zone, resulting in a wavier deformation pattern in this area. More frequent bouncing of thermomechanical waves in the double-layered film (a larger value of Y), in addition, renders a lower magnitude of U' in comparison with that in Fig. 6(b).

The ultrafast deformation pattern is not as sensitive to parameters K or C. A larger value of K, implying a larger value of conductivity or a smaller value of heat capacity of electrons at room temperature, reduces the magnitude of U' by as much as one order of magnitude, as shown in Fig. 7(c) for $K = 64.1$. A larger value of C,

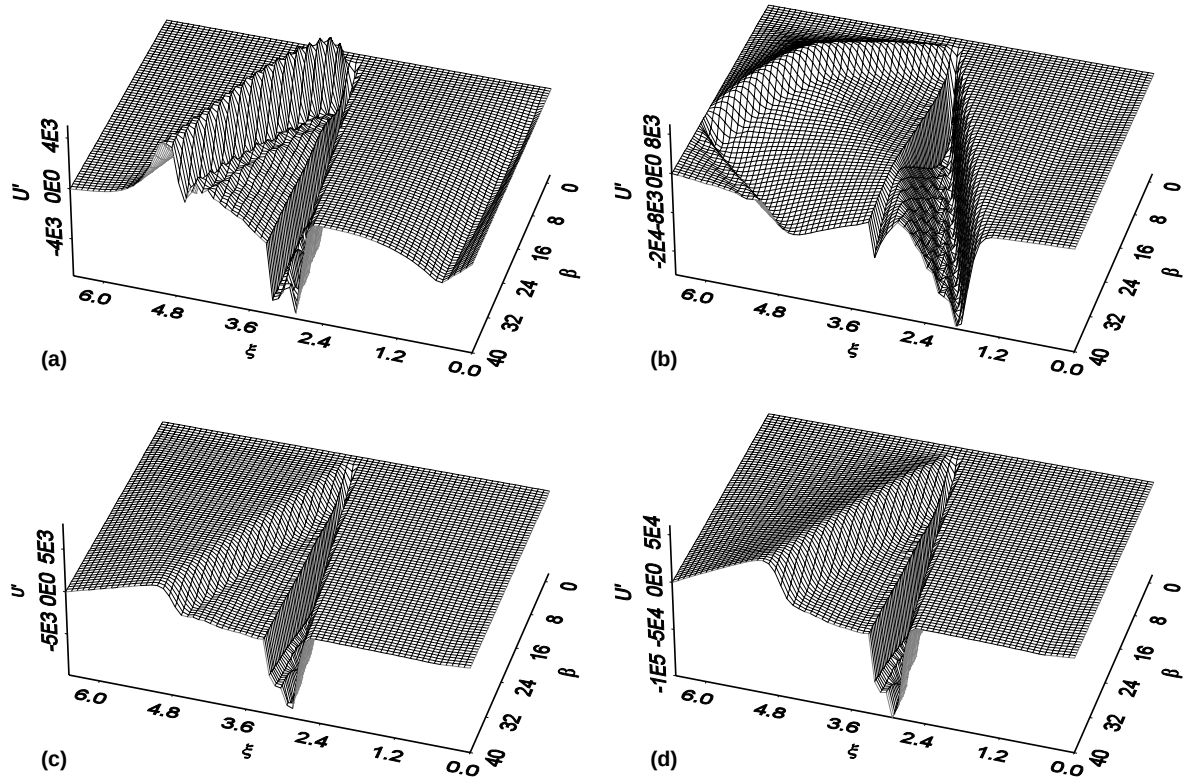

Fig. 7. Effects of (a) $H = 12.4$, (b) $Y = 1.71 \times 10^{-3}$, (c) $K = 64.10$, and (d) $C = 8.4 \times 10^{-2}$ on the ultrafast deformation in the double-layered films. All other data are same as those in Table 1.

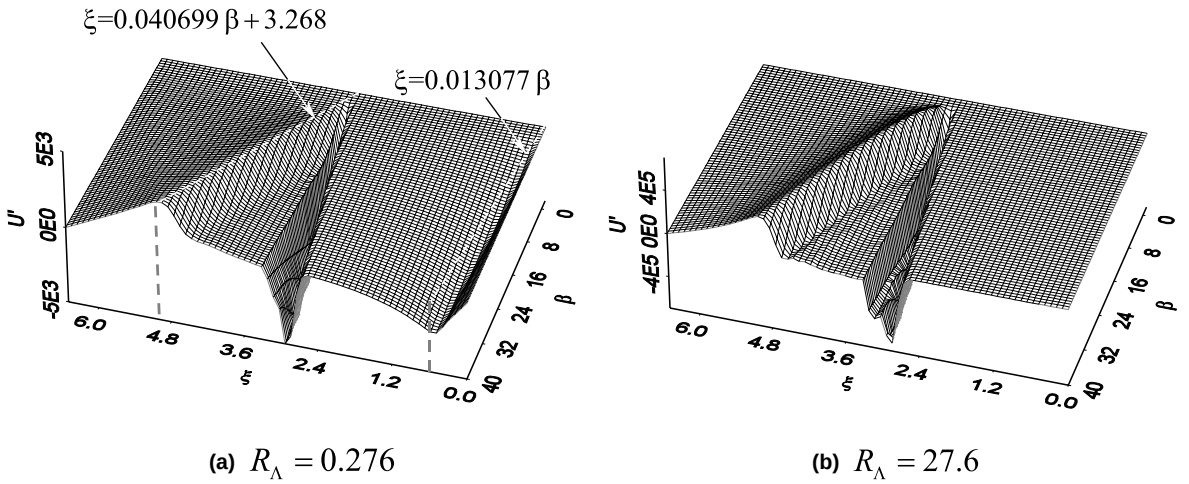

Fig. 8. Effects of R_Λ on the ultrafast deformation in the double-layered films. All other data are same as those in Table 1.

implying a larger value of conductivity of electrons at room temperature or a smaller value of the lattice conductivity, on the other hand, produces a stronger compressive strain near the interface, as shown in Fig. 7(d) for $C = 8.4 \times 10^{-2}$. The overall patterns of ultrafast deformation in Figs. 7(c) and (d), however, are very close to that shown in Fig. 6(b), the base curve with $K = 6.41$ and $C = 8.4 \times 10^{-3}$.

5.5. Effects of property ratios

In addition to the parameters H, Y, K, and C that characterize the gold layer (medium (I)), the ultrafast deformation also depends on seven property ratios defined in Eq. (21). Their effects may be coupled with those of H, Y, K, and C due to involvement of common properties in their definitions. A smaller value of R_E, for example, is equivalent to a larger value of $E^{(\mathrm{I})}$, which, in turn, implies a larger value of Y investigated earlier in Fig. 7(b). A similar argument can be applied to the effect of R_ρ, where effect of a larger value of R_ρ resembles to that of a larger value of Y. As the value of R_E decreases or the value of R_ρ increases, therefore, a similar pattern of ultrafast deformation to that shown in Fig. 7 would be expected. The property ratios of R_k, R_{C_e}, R_{C_l}, and R_G all fall into the same category.

Effect of R_Λ needs to be explored separately because the parameter Λ is absorbed in the reference phonon displacement shown in Eq. (13). Again, Fig. 6(b) with $R_\Lambda = 2.76$ is the based curve used for comparisons. As the value of R_Λ decreases, $R_\Lambda = 0.276$ shown in Fig. 8(a), the magnitude of U' decreases accordingly, with the two characteristic wavefronts now clearly shown due to the closer levels of compressive strains developed in the double-layered film. As the value of R_Λ increases, $R_\Lambda = 27.6$ shown in Fig. 8(b), on the other hand, the magnitude of U' increases accordingly, reaching the order of 10^5 at the peaks of the compressive (near the interface) and tensile strains (at the characteristic wavefront $(\xi, \beta) \cong (4.89, 40)$). To prevent significant straining in the laser heated double-layered film, therefore, it is desirable to select a metal film with a largest possible value of $\Lambda(\Lambda^{(\mathrm{I})})$ to resist direct laser heating, while selecting a padding layer with a smallest possible value of $\Lambda(\Lambda^{(\mathrm{II})})$ to reduce the ratio of R_Λ.

6. Conclusion

The hot-electron blast produced during the first few tenths of a picosecond is a direct result of non-equilibrium heating induced by femtosecond lasers. It results in ultrafast deformation of acoustic phonons in the picosecond domain, which has not received as much attention as ultrafast heating in microscale heat transfer. Dynamical equations of motion (for ultrafast deformation) have been integrated with the parabolic phonon–electron interaction model (for ultrafast heating) to study the effect of the hot-electron blast in multi-layered thin metal films. Special feature includes maximum compressive strains developed at the interface between dissimilar media, as well as the rapid alteration from compression to tension in the neighborhood of the characteristic wavefront. The latter is noteworthy for damage prevention since metals are usually weaker in resisting tension than compression. Since the characteristic wavefront is always located *within* the medium, tensile straining thereby may produce *internal* damage within the laser-heated films. Severe compressive straining developed in the vicinity of the interface, on the other hand, may result in shear failure that is the major cause for delamination in multi-layered films. The in-

terwoven tension and compression induced by the hot-electron blast makes the prediction for damage in thin metal films extremely complicated, which needs further explorations along with the high-rate data of yield strength, fracture toughness, and shear strength for metals in general.

Effect of deformation plays a more important role in sub-micron films when heated by a femtosecond laser. For the laser fluence on the order of 10^2–10^3 J m^{-2}, the resulting displacement reach a fraction of the film thickness of the order of 0.1 μm. Simultaneous considerations of the deformation effect, therefore, seem necessary in describing the mechanisms of ultrafast heating in thin metal films. It should be reminded, however, that the present model is only valid for ultrafast deformation of acoustic phonons, under the assumption that the electron temperature is significantly lower than the Fermi temperature during the picosecond transient. For intense heating that produces hot electrons close to the Fermi temperature, or for even faster deformation of optical phonons in the femtosecond domain, the blasting force becomes much more involved than a simple gradient of electron-temperature squared. Renormalization of metal lattices (which results in electron-temperature-dependent elastic moduli due to electron looping in metal lattices) and ultrafast lattice restoration (induced by the additional deformation potential vector) are essential physical mechanisms that need to be accommodated. In most cases, the non-equilibrium partition functions of electrons and phonons need to be further examined by the Boltzmann transport equation to determine the functional forms that are appropriate for an engineering analysis posed in the present work.

References

[1] J. Opsal, The application of thermal wave technology to thickness and grain size of aluminum films, in: Metallization: Performance and Reliability Issues for VLSI and ULSI, SPIE, Vol. 1596, 1991, pp. 120–131.

[2] A. Mandelis, S.B. Peralta, Thermal-wave based materials characterization and nondestructive evaluation of high-temperature superconductors: a critical review, in: R. Kossowsky (Ed.), Physics and Materials Science of High Temperature Superconductors II, Kluwer Academic Publishers, Boston, MA, 1992, pp. 413–440.

[3] J.A. Knapp, P. Børgesen, R.A. Zuhr (Eds.), Beam–Solid Interactions: Physical Phenomena, Mater. Res. Soc. Symp. Proc., vol. 157, Materials Research Society, Pittsburgh, PA, 1990.

[4] D.J. Elliot, B.P. Piwczyk, Single and multiple pulse ablation of polymeric and high density materials with excimer laser radiation at 193 nm and 248 nm, Mater. Res. Soc. Symp. Proc. 129 (1989) 627–636.

[5] C.P. Grigoropoulos, Heat transfer in laser processing of thin films, in: C.L. Tien (Ed.), Annual Review of Heat Transfer, vol. V, Hemisphere, New York, 1994, pp. 77–130.

[6] J. Narayan, V.P. Gosbole, G.W. White, Laser method for synthesis and processing of continuous diamond films on nondiamond substrates, Science 52 (1991) 416–418.

[7] J.M. Hopkins, J. Sibbett, Ultrashort-pulse lasers: big payoffs in a flash, Sci. Am. 283 (2000) 72–79.

[8] D.Y. Tzou, Ultrafast heat transport: the lagging behavior, Invited paper in Session of Gigahertz to Terahertz Photonics, 44th SPIE's Annual Meeting, July 18–22, Denver, CO, 1999.

[9] D.Y. Tzou, Ultrafast transient behavior in microscale heat/mass transport, Advanced Photon Source Millennium Lecture Series, Argonne National Laboratories, March 1, Chicago, IL, 2000.

[10] D.Y. Tzou, Microscale heat transfer and fluid flow, Plenary Lecture and Panel of Terahertz and Gigahertz Electronics and Photonics, 45th SPIE's Annual Meeting, July 30–August 4, San Diego, CA, 2000.

[11] DOE (Department of Energy) BES (Basic Energy Sciences) Workshop, 1999, Complex Systems – Science for the 21st Century. Available from: www.sc.doe.gov/production/bes/complexsystems.htm.

[12] DOE (Department of Energy) BES (Basic Energy Sciences) Workshop, 1999, Nanoscale Science, Engineering, and Technology – Research Direction. Available from: www.sc.doe.gov/production/bes/nanoscale.html.

[13] C. Momma, S. Nolte, B.N. Chichkov, F.V. Alvensleben, A. Tunnermann, Precise laser ablation with ultrashort pulses, Appl. Surf. Sci. 109 (1997) 15–19.

[14] M.D. Shirk, P.A. Molian, A review of ultrashort pulsed laser ablation of materials, J. Laser Appl. 10 (1998) 18–28.

[15] H.E. Elsayed-Ali, T.B. Norris, M.A. Pessot, G.A. Mourou, Time-resolved observation of electron–phonon relaxation in copper, Phys. Rev. Lett. 58 (1987) 1212–1215.

[16] S.D. Brorson, J.G. Fujimoto, E.P. Ippen, Femtosecond electron heat-transport dynamics in thin gold film, Phys. Rev. Lett. 59 (1987) 1962–1965.

[17] T.Q. Qiu, T. Juhasz, C. Suarez, W.E. Bron, C.L. Tien, Femtosecond laser heating of multi-layered metals – II. Experiments, Int. J. Heat Mass Transfer 37 (1994) 2799–2808.

[18] M.I. Kaganov, I.M. Lifshitz, M.V. Tanatarov, Relaxation between electrons and crystalline lattices, Sov. Phys. JETP 4 (1957) 173–178.

[19] S.I. Anisimov, B.L. Kapeliovich, T.L. Perel'man, Electron emission from metal surfaces exposed to ultra-short laser pulses, Sov. Phys. JETP 39 (1974) 375–377.

[20] T.Q. Qiu, C.L. Tien, Short-pulse laser heating on metals, Int. J. Heat Mass Transfer 35 (1992) 719–726.

[21] T.Q. Qiu, C.L. Tien, Heat transfer mechanisms during short-pulse laser heating of metals, ASME J. Heat Transfer 115 (1993) 835–841.

[22] T.Q. Qiu, C.L. Tien, Femtosecond laser heating of multi-layered metals – I. Analysis, Int. J. Heat Mass Transfer 37 (1994) 2789–2797.

[23] D.Y. Tzou, A unified field approach for heat conduction from micro- to macro-scales, ASME J. Heat Transfer 117 (1995) 8–16.

[24] D.Y. Tzou, The generalized lagging response in small-scale and high-rate heating, Int. J. Heat Mass Transfer 38 (1995) 3231–3240.

[25] D.Y. Tzou, Experimental support for the lagging response in heat propagation, AIAA J. Thermophys. Heat Transfer 9 (1995) 686–693.
[26] D.Y. Tzou, Macro- to Microscale Heat Transfer: The Lagging Behavior, Taylor & Francis, Washington, DC, 1997.
[27] D.Y. Tzou, J.K. Chen, Thermal lagging in random media, AIAA J. Thermophys. Heat Transfer 12 (1998) 567–574.
[28] D.Y. Tzou, K.S. Chiu, Temperature-dependent thermal lagging in ultrafast laser heating, Int. J. Heat Mass Transfer 44 (2001) 1725–1734.
[29] J.K. Chen, J.E. Beraun, Numerical study of ultrashort laser pulse interactions with metal films, Numer. Heat Transfer A: Applications 40 (1) (2001) 1–20.
[30] M.D. Perry, B.C. Staurt, P.S. Banks, M.D. Feit, V. Yanovsky, A.M. Rubenchik, Ultrashort-pulse laser machining of dielectric materials, J. Appl. Phys. 85 (1999) 6803–6810.
[31] L.A. Falkovsky, E.G. Mishchenko, Electron–lattice kinetics of metals heated by ultrashort laser pulses, J. Exp. Theoret. Phys. 88 (1999) 84–88.
[32] D.Y. Tzou, J.K. Chen, J.E. Beraun, Ultrafast deformation in femtosecond laser heating on metals, 2001 IMECE, Session of Microscale Energy Systems, New York, November 6–11, 2001.
[33] L.A. Falkovsky, E.G. Mishchenko, Surface excitations in metals: Brillouin and Raman light scattering, Phys. Rev. B 51 (1995) 7239–7249.
[34] E.Zh. Mishchenko, L.A. Falkovsky, Long-wavelength optical phonons: damping, surface oscillations, and Raman scattering, J. Exp. Theoret. Phys. 80 (1995) 531–538.
[35] J.K. Chen, W.P. Latham, J.E. Beraun, Axisymmetric modeling of femtosecond-pulse laser heating on metal films, J. Numer. Heat Transfer (in press).
[36] The IMSL Fortran 90 MP Mathematics and Statistics Libraries (F90 MP), Visual Numerics Inc., Houston, TX.